AGU PUBLICATIONS

Geophysical Research Letters

RESEARCH LETTER
10.1002/2017GL075207

Key Points:
- Impact simulations were used to determine depth of origin of material exposed within the peak ring in lunar basins
- Basin size-dependent trends show depth of origin for a range of lunar impact basins, up to the upper mantle
- Basin size-dependent relationships help determine lunar composition and stratigraphy

Supporting Information:
- Supporting Information S1

Correspondence to:
K. Miljković,
katarina.miljkovic@curtin.edu.au

Citation:
Miljković, K., Lemelin, M., & Lucey, P. G. (2017). Depth of origin of the peak (inner) ring in lunar impact basins. *Geophysical Research Letters, 44*, 10,140–10,146. https://doi.org/10.1002/2017GL075207

Received 8 AUG 2017
Accepted 29 SEP 2017
Accepted article online 9 OCT 2017
Published online 19 OCT 2017

Depth of Origin of the Peak (Inner) Ring in Lunar Impact Basins

Katarina Miljković[1], Myriam Lemelin[2,3], and Paul G. Lucey[2]

[1]Department of Applied Geology, Curtin University, Perth, Western Australia, Australia, [2]Hawai'i Institute of Geophysics and Planetology, Department of Geology and Geophysics, School of Ocean and Earth Science and Technology, University of Hawai'i at Mānoa, Honolulu, HI, USA, [3]Earth and Space Science and Engineering, Department Lassonde School of Engineering, York University, Toronto, Ontario, Canada

Abstract Numerical modeling of the peak-ring basin formation showed that the peak-ring forms from the material that is part of the central uplift outwardly thrust over the inwardly collapsing transient crater rim. Simulations of the lunar basin formation showed that the peak or inner ring in peak ring or multiring basins, respectively, is composed of the overturned crust and deep-seated material, possibly from the upper mantle. Numerical impact simulations were used to trace the depth of origin of material exposed within the peak (or inner) ring. We estimate the scaling trends between basin size and the depth of origin of material exposed within the ring. We also report on the likely crust, mantle, and projectile abundances exposed within the ring. Quantifying the excavation depths during the formation of the peak or inner ring provides a step toward understanding the lunar crust and mantle stratigraphy.

1. Introduction

Large impact craters, or impact basins, can be divided in two categories based on their morphology and ring formation process: the peak-ring and multiring basins. This crater morphology is present on all rocky bodies in the solar system. The transition from the complex crater to peak-ring to multiring basin scales inversely with the parent body gravity (Melosh, 1989). On the Moon, the onset diameters for the formation of peak-ring basins are ~150 km and ~300 km for the multiring basins (e.g., Wood & Head, 1976). Peak-ring basins (e.g., Schrödinger) have a single ring located within their main topographic rim, and multiring basins (e.g., Orientale) have multiple ring-like features (e.g., Hartmann & Kuiper, 1962; Melosh, 1989; Spudis, 1993).

The dynamic theory for the peak-ring formation suggested that the peak ring likely forms through the interaction of two collapse regimes: (1) the outward collapse of the uplift of the underlying material at the bottom of the transient crater and (2) the inward collapse of the transient crater wall (e.g., Murray, 1980). This theory was supported by (a) numerical impact modeling that showed that the peak ring should be composed of deeply derived material and that the ring stratigraphy exhibits an overturned structure (e.g., Collins et al., 2002), (b) detailed mineral mapping of lunar impact basins (Baker et al., 2016; Kring et al., 2016), and (c) rock sample analyses obtained by the drilling expedition to the peak ring of the Chicxulub crater (Morgan et al., 2016). Furthermore, recent numerical modeling of the formation of the multiring Orientale basin (Potter, Kring, & Collins, 2013; Johnson et al., 2016) demonstrated that the inner ring in multiring basins forms via the same mechanism as peak rings in peak-ring basins.

Previous impact studies have mainly focused on quantifying the maximum depth of excavation during crater formation. According to the Maxwell's *Z*-model of the excavation flow (Melosh, 1989) and recent numerical impact modeling work (e.g., Potter et al., 2015), the maximum depth of excavation in lunar basins was estimated to be 0.12 D_{tr}, where D_{tr} is the transient crater diameter. Although, Potter, Kring, Collins, and Kiefer et al. (2013) quantified the stratigraphic uplift during basin formation, there is no clear relationship between the depth of origin of the material exposed in the peak or inner ring and impact basin size.

In this work, we use the results from numerical impact simulations to determine the scaling trends for the depth of origin of materials exposed within peak and inner rings in lunar peak ring and multiring basins, respectively. We also report on the crust, mantle, and projectile abundances exposed within the ring, as a function of impact condition and target properties.

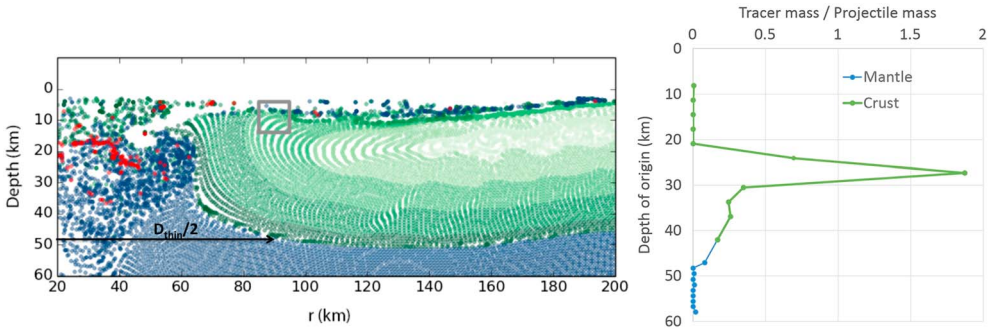

Figure 1. (left) Lunar impact basin made by a 30 km projectile impacting at 17 km/s shown in vertical cross section. The target temperature profile is "intermediate." The crust (shown by green tracer particles) is 45 km thick, overlaying the mantle (shown in blue tracer particles). Tracers shown in red represent residues of the projectile. The gray box is centered at the radius of the peak ring, which also corresponds to the radius of the crustal thinning ($D_{thin}/2$); (right) relative mass distribution of tracer particles and their respective depth of origin, extracted from the sampling box shown on the left. The crustal component shown in green and mantle component in blue.

2. Method

To simulate the lunar impact basin formation, we used the iSALE-2D hydrocode, a multimaterial, multirheology finite difference shock-physics code used for simulating impact processes in geologic media (Amsden et al., 1980; Collins et al., 2004; Wünnemann et al., 2006). This code has been extensively used for modeling impact basin formation on the Moon (Johnson et al., 2016; Melosh et al., 2013; Miljković et al., 2013, 2015, 2016; Potter et al., 2012; Potter, Kring, & Collins, 2013; Potter, Kring, Collins, Kiefer et al., 2013; Potter et al., 2015; Zhu et al., 2015) and was benchmarked against other hydrocodes (Pierazzo et al., 2008).

We investigated impacts made by 15, 30, 45, and 60 km diameter impactors hitting the Moon at an average speed of 17 km/s (Le Feuvre & Wieczorek, 2011), as used and justified in Miljković et al. (2013). The average lunar crustal thickness on the nearside hemisphere is 34 km, and 43 km on the farside hemisphere (Wieczorek et al., 2013). Therefore, the Moon was assumed to be a flat target made of a 30 or 45 km thick crust overlaying mantle. To represent the thermal state of the Moon at the time lunar basins had formed, we applied "cold," "intermediate," and "hot" target temperature profiles, as described in Miljković et al. (2013, 2015, 2016), typical for the lunar farside, nearside (except the PKT), and the PKT region, respectively. The crust (modeled using basalt ANEOS), mantle, and projectile (both modeled using dunite ANEOS) used material models from Miljković et al. (2013, 2015, 2016). These sets of impactor and target properties cover the entire size range of lunar basins, except the South Pole-Aitken (SPA) basin and possibly Imbrium. The reason for excluding the largest lunar basins was because of difficulty in modeling the formation of the inner ring in such large basins due to the very large amount of melt forming in the center of the basin.

The depth of origin of the material exposed in the peak or inner ring was tracked using Lagrangian tracer particles placed in every cell of the Eulerian numerical mesh. Numerical cell size was set to 1.5 by 1.5 km in all simulations, which provided sufficient resolution to observe the peak-ring formation process. Given the resolution, we can properly resolve the combination of the collapse of the transient crater, stratigraphic uplift of the transient crater floor, and collapse of the overturned crustal material that contribute to the peak-ring formation. The trajectory of each tracer was recorded during the basin formation process, so that the initial location of the material can be determined at the end of a simulation. We identified a region of 10 km radial distance (at final surface level) by 10 km depth centered at the radius of the peak ring (gray box, Figure 1), and we analyzed all tracers located in this region. This method allowed for sampling a statistically significant number of tracers that will provide a good representation of the possible range of the material's depth of origin, for all materials exposed within the ring. We also found that the tracer sample box was moderately insensitive to its size. If the sample box increases by 100% in both radial and vertical directions, it still produced less than 10% variation in the mean depth of origin of the materials as well as the crust-mantle proportions.

Considering all numerical simulations were made in 2-D, it was important to estimate the mass of each cell that tracers represented in 3-D. All numerical models were cylindrically symmetric; therefore, the volume of each cell was calculated as a volume of a torus around the vertical axis. Thickness of the torus

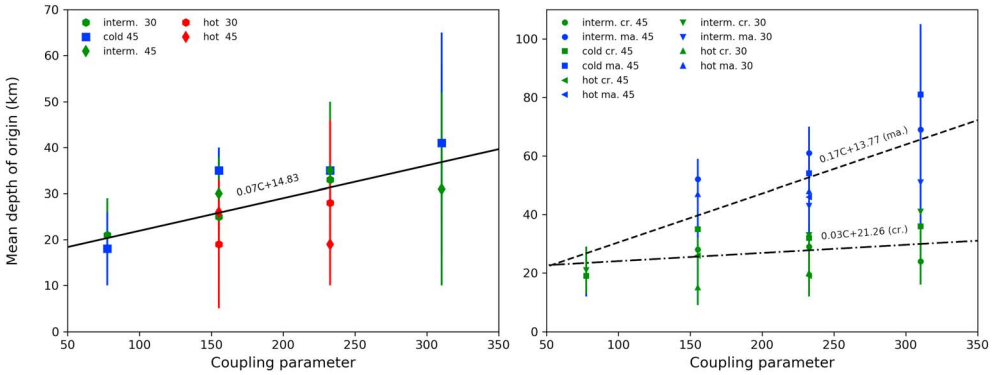

Figure 2. (a) (left) The mean depth of origin of material exposed within the peak or inner ring for a range of basin sizes, represented via the coupling parameter ($LV^{0.58}$, where L is the projectile diameter in km and V speed in km/s). The range of values (50–350) for the coupling parameter shown in x axis corresponds to D_{thin} values increasing from 50 to 500 km, according to the scaling trends developed in Miljković et al. (2016). The vertical error bars denote 1σ standard deviation from the sampled tracer depths. The symbols shown in red, green, and blue mark the simulations made into a "hot," "intermediate," and "cold" targets. (b) (right) The mean depth of origin of the crust and mantle materials exposed within the peak or inner ring for a range of basin sizes, respectively. The green symbols denote the crustal component, and the blue symbols denote the mantle. The different symbol shapes mark different crustal thicknesses (30 or 45 km).

corresponded to the numerical cell size. The volume of each tracer depended on its initial distance from the symmetry axis; the further it is from the symmetry axis, the larger the tracer (torus) volume. Depending on whether the cell represented the crust or the mantle materials, the respective masses for each tracer were calculated.

An example of a numerical simulation of lunar basin formation is shown as a vertical 2-D slice of half-basin in Figure 1 (left). The material exposed within the peak ring originated from various depths, based on the analysis of approximately 100 tracer particles from the 10 by 10 km sampler (gray box in Figure 1, left). Zooming into the gray box marked in Figure 1 (left), Figure 1 (right) shows the range of depths from which the material that formed the peak or inner ring originated from. The mass of tracers was normalized to the projectile mass.

The location of the tracer sampler box (Figure 1) is at the peak-ring radius as determined from the gravity signature and defined by Neumann et al. (2015). We avoid using the transient cavity diameter (D_{tr}) as a measure of the crater size, because it is not possible to determine D_{tr} in basins using any topographic feature (e.g., Zuber et al., 2016). Instead, we use the peak/inner-ring diameter D_{ring}. For some basins, even this ring diameter cannot be determined from topographic data, but it is possible to infer it from the gravity data. Neumann et al. (2015) showed that the peak-ring diameter and the diameter of the Bouguer gravity high in peak ring and some multiring basins follow a 1:1 ratio. This way, we can constrain the size of lunar impact basins. The Bouguer gravity high reported by Neumann et al. (2015) as the peak/inner ring diameter also corresponds to the diameter of the crustal thinning D_{thin} defined as twice the distance from the point of impact to the location where the crustal thickness becomes equal to the preimpact crustal thickness. The diameter of the crustal thinning has been used as a measure of basin size in previous works Miljković et al. (2013, 2015, 2016).

3. Results

Numerical impact simulations used in this work showed the same formation mechanism for the peak ring as reported in past works (e.g., Baker et al., 2016; Collins et al., 2002; Kring et al., 2016). Here we present the following: the mean depth of origin of materials exposed within peak ring in peak-ring basins or inner ring in multiring basins, as a function of impact and target conditions; the range of possible depths of origin for the crustal and mantle materials exposed within peak or inner ring in peak ring or multiring basins, respectively; mass abundances of the crust and mantle material exposed within the ring, as a function of impact and target conditions; synthesis of the results into scaling trends focusing on the mean depth of origin and the crust-mantle mass abundances, as a function of the preimpact crustal thickness; and application of the scaling trends on the range of lunar peak ring to multiring impact basins that are within the investigated range of impact size and crustal thickness.

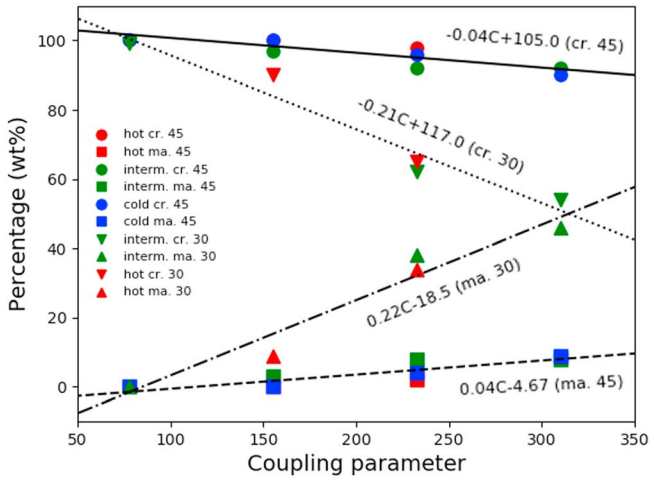

Figure 3. The proportions of the crust and mantle mass abundances exposed within the peak or inner ring as a function of impact size represented by the coupling parameter for 30 and 45 km thick crust. There are two data points from each simulation, one denoting the crustal and the other mantle abundances (in wt % adding up to ~100). The symbols shown in red, green, and blue mark the simulations made into a "hot," "intermediate," and "cold" targets. "cr." and "ma." denote the crust and mantle components, respectively.

3.1. Scaling Trends

The peak (inner) ring forms through a complex and violent process, composed of the collapsing central uplift and slumping of the ejected and overturned crust. Therefore, defining the depth of origin of the material exposed in these rings is not a trivial task. However, in this study, we produced over-encompassing and simplified scaling trends that relate: (a) the basin size with the mean depth of origin of material exposed within the peak (inner) ring and (b) the basin size with the crust and mantle abundances exposed within the ring, for the purpose of a better understanding of the lunar composition. The scaling trends presented here are only applicable to lunar basins because the formation of impact basins is dependent on the properties of the parent body.

Figure 2a shows the mean depth of origin of material exposed within the peak (or inner) ring for a range of basin sizes, represented via the coupling parameter, C ($C = LV^{0.58}$, where L is the projectile diameter in km and V speed in km/s, as used in Miljković et al., 2016). The vertical error bar denotes 1σ standard deviation in the range of depths exposed at the surface (as sampled in the tracer box in the simulations).

Only one basin size-depth scaling trend was produced for the entire Moon (equation (1)), even though recent literature demonstrated the importance of the thermal properties on basin formation (Miljković et al., 2013, 2015, 2016; Potter et al., 2012, 2015). This was because of the wide range of possible depths for each basin that was larger than the mean depth ranges affected by the lunar thermal properties. This is demonstrated in Figure 2a by labeling the simulation results according to the applied thermal gradient. The thermal gradients used were from Miljković et al. (2013, 2015, 2016).

Figure 2b also shows the mean depth of origin of the material exposed within the ring but separated between the mean depth of materials coming from the crust and the mantle, for two different crustal thicknesses (30 and 45 km). Similarly, the standard deviation for the depth of origin (marked by the vertical error bar) is larger than difference between the mean depths coming from these two crustal thicknesses; therefore, we derive only one scaling trend for the mean depth of origin of materials coming from the crust and mantle, respectively.

The mean depth of origin of materials exposed within the ring starts at about 20 km and reaches up to about 40 km or middle to lower crust. The mean depth of the crustal material is fairly constant at approximately 24–30 km for the investigated lunar basin size range. However, the mean depth of the mantle material increases significantly with impact size. The data shown in Figures 2 and 3 are listed in Table S1 in the supporting information, and scaling trends are shown as equations (1)–(3). The depth is calculated in km.

$$\text{Depth (total)} = 0.07C + 14.83 \quad (1)$$

$$\text{Depth (crust)} = 0.03C + 21.26 \quad (2)$$

$$\text{Depth (mantle)} = 0.17C + 13.77, \quad (3)$$

for $C = LV^{0.58}$.

In summary, equations (1)–(3) do not include regional variation in lunar thermal properties at the time basins formed or the differences in the crustal thickness across the lunar surface. Therefore, these equations should be used as a first-order estimate of a relationship that has not been estimated in previous works.

Figure 2a shows that the mean depth of origin of peak tracer material is dependent on the basin size, but only weakly on parameters such as the thermal gradient and the crustal thickness. When separated into crustal and mantle components, only the mantle component depth of origin shows a strong dependence on basin size (Figure 2b). However, Figure 3 shows that the relative abundance of crust and mantle as a function of crater size is strongly dependent on crustal thickness. The crustal component is dominant for the entire

Table 1
Mean Depth of Origin and Mass Abundances of Materials Exposed Within the Peak or Inner Ring for a Selection of Lunar Impact Basins

Basin name	C	H (km)	d (km)	dc (km)	dm (km)	cr. and ma. (wt %), 30	cr. and ma. (wt %), 45
Nearside hemisphere							
Serenitatis	427	26 ± 8	45	34	87	cr: ~27 ma: ~75	cr: ~88 ma: ~12
Crisium	336	28 ± 8	38	31	71	cr: ~46 ma: ~55	cr: ~91 ma: ~9
Nectaris	295	29 ± 7	35	30	64	cr: ~55 ma: ~45	cr: ~93 ma: ~7
Humorum	271	30 ± 2	34	29	60	cr: ~60 ma: ~41	cr: ~94 ma: ~6
Humboldtianum	232	28 ± 8	31	28	53	cr: ~68 ma: ~32	cr: ~96 ma: ~5
Grimaldi	125	31 ± 7	24	25	35	cr: ~91 ma: ~9	cr: ~100 ma: <1
Farside hemisphere							
Orientale	271	36 ± 9	34	29	60	cr: ~60 ma: ~41	cr: ~94 ma: ~6
Mendel-Rydberg	238	35 ± 8	31	28	55	cr: ~63 ma: ~34	cr: ~95 ma: ~5
Moscoviense	238	36 ± 11	31	28	55	cr: ~67 ma: ~34	cr: ~95 ma: ~5
Freundlich-Sharonov	261	42 ± 9	33	29	58	cr: ~62 ma: ~39	cr: ~94 ma: ~6
Apollo	222	29 ± 9	30	28	52	cr: ~70 ma: ~30	cr: ~96 ma: ~4
Hertzsprung	207	48 ± 7	29	27	49	cr: ~73 ma: ~27	cr: ~97 ma: ~4
Korolev	158	51 ± 5	26	26	41	cr: ~83 ma: ~16	cr: ~99 ma: ~2
Schrödinger	158	27 ± 5	26	26	41	cr: ~84 ma: ~16	cr: ~98 ma: ~2
Mendeleev	149	40 ± 4	25	25	39	cr: ~86 ma: ~14	cr: 99 ma: 1
Lorentz	141	35 ± 5	25	25	38	cr: ~87 ma: ~13	cr: 99 ma: 1

Note. Data for the coupling parameter C and preimpact crustal thickness H were from Miljković et al. (2016). *d* is the total mean depth of origin; dc and dm are the mean depth of origin of the crust and mantle component; "cr." and "ma." denote the proportional mass abundance of the crust and mantle component separately, for the 30 km and 45 km preimpact crustal thickness, respectively.

range of explored basin sizes when formed in the 45 km crust. However, the mantle component becomes increasingly dominant with the increase in basin sizes when formed in the 30 km crust. The projectile contribution in all simulations was found to be <1 wt %.

Equations (4) and (5) show the proportions (in wt %) for the crust and mantle component, respectively, for the 30 km crust and equations (6) and (7) for the 45 km crust. These linear fits are applicable to the coupling parameter that ranges from ~80 to about 400, which includes nearly all lunar basins (excluding the South Pole-Aitken basin and possibly Imbrium). Equations (4)–(7) cannot be used beyond the indicated basin size range (presented by the coupling parameter), as they would produce invalid proportions. Basins forming smaller than investigated here are likely to form as protobasins or complex craters, and larger basins cannot have their inner ring simulated accurately due to the large amount of melt produced in the simulation. This could also indicate a different mechanism or a lack of inner ring in the largest lunar basin (for example, the SPA basin).

$$P\,(\text{crust}) = -0.21C + 117 \tag{4}$$

$$P\,(\text{mantle}) = 0.22C - 18.5, \tag{5}$$

for the 30 km thick crust.

$$P\,(\text{crust}) = -0.04C + 105 \tag{6}$$

$$P\,(\text{mantle}) = 0.04C - 4.67, \tag{7}$$

for the 45 km thick crust.

3.2. Depth of Origin of Peak (Inner) Rings in Lunar Basins

The Lunar impact basin catalogue of Neumann et al. (2015), based on GRAIL gravity data, lists about 60 confirmed impact basins. Table 1 lists 15 representative basins, based on their crustal thickness being within the investigated range of approximately 30 to 45 km. The list of remaining investigated lunar basins is provided in Table S2.

In Table 1, *C* is the coupling parameter and *H* is the preimpact crustal thickness. The values for *C* and *H* were used from Miljković et al. (2016). Equations (1)–(7) were applied respectively to estimate the depth of origin of materials exposed within their peak or inner ring, as well as crust-mantle mass abundances. Parameters *d*, *dc*, and *dm* are respectively the mean depth of origin of material exposed within the ring, material only from the crust, and material only from the mantle. Abundances of the crust and the mantle exposed within the peak

ring are shown as "cr." and "ma.," respectively. Numbers 30 and 45 denote the 30 and 45 km preimpact crustal thickness used in simulations. We calculate the mass abundances for both crustal thicknesses; however, the likely values are the ones corresponding to the closest value of the preimpact crustal thickness. The mass abundances are shown as very approximate estimates.

The investigation of the Schrödinger basin in Kring et al. (2016) reported that the material exposed within the peak ring is majorly of the crustal origin, from 20 to 30 km depth, and with the maximum excavation depth of 19–24 km, depending on the assumed crustal thickness. This work agrees with Kring et al. (2016). As shown in Table 1, the Schrödinger basin was estimated to have its peak ring composed of >80% crustal material, with the mean depth of origin at 26 km.

The maximum excavation depth for lunar basins is estimated to correspond to 0.12 D_{tr} (e.g., Melosh, 1989; Potter et al., 2015), where D_{tr} is the diameter of the transient crater. Replacing that relation in equations shown in Table 1 in Miljković et al. (2016), and including the range of basins size values (from ~80 km to ~600 km in the crustal thinning diameter; Miljković et al., 2016), we calculated the maximum excavation depth to be between 10 km for the smallest and up to 60 km for the largest lunar basins. Figure 2a shows that the possible range of depth of origin of the peak/inner ring can be between 20 and 40 km. The maximum excavation depth is approximately half the maximum depth of origin of materials exposed within the ring. This also suggests that our studies are in agreement.

Yamamoto et al. (2010) reported that several basins on the lunar nearside and the Moscoviense basins on the lunar farside could have excavated mantle materials because of strong olivine signatures detected in association with these basins. Miljković et al. (2013) supported this study by a numerical investigation of basin formation that could have excavated mantle materials. However, that study only reported dominant surface-only mantle exposures (thicker than a couple of numerical cells with mantle cell concentration being >50%). In this study, all basins reported in Miljković et al. (2013) to have mantle exposure were also reconfirmed to have mantle exposures within peak rings (top 10 km surface thickness).

4. Conclusion

Numerical impact simulations showed that the peak or inner ring is the only morphological feature in an impact basin that contains deep-seated material, not including the main melt pool, which is almost always buried by the crustal inflow or subsequent mare volcanism. For the majority of lunar impact basins, the mean depth of origin of the material exposed within the peak or inner ring is about 20–40 km, and this range is in agreement with previous studies reporting on excavation depths (e.g., Melosh, 1989, Potter et al., 2015). Within the peak or inner ring, the crustal contribution persistently originates from the middle to lower crust, while the depth of origin of the mantle component increases with the increase in basin size. However, the proportion of the crust and mantle abundances exposed within the ring is strongly dependent on the preimpact crustal thickness.

Scaling trends derived in this work can be used to help determine the lunar crust and mantle stratigraphy, for the majority of lunar basins except SPA and basins within it that likely formed in very thin crust (outside of our investigated crustal thickness range). Even though the lunar crust had been heavily cratered particularly during the first 700 Myr, it should still be possible to gain some insights into the crustal stratigraphy by comparing these findings with compositional remote sensing data. Our work is also aligned with recent remote sensing and numerical modeling works focused on the Schrödinger (Kramer et al., 2013; Kring et al., 2016) and Orientale basins (Potter, Kring, & Collins, 2013, Cheek et al., 2013, Johnson et al., 2016).

The peak rings of the largest nearside basins are perfect candidate basins for sampling lunar mantle (e.g., Crisium). Smaller basins located in the thicker crust (on the farside hemisphere), including the Schrödinger basin, would represent perfect candidates for sampling lower crust. These locations should be included in objectives of future lunar missions.

Acknowledgments
We gratefully acknowledge the developers of iSALE-2D, including Gareth Collins, Tom Davison, Kai Wünnemann, Dirk Elbeshausen, Boris Ivanov, and Jay Melosh. The data used in this study are attached as supporting information and are also available upon request from the main author (katarina.miljkovic@curtin.edu.au).

References

Amsden, A. A., Ruppel, H. M., & Hirt, C. W. (1980). SALE: A simplified ALE computer program for fluid flow at all speeds. Rep. LA-8095, pp. 105. New Mexico: Los Alamos National Laboratories.

Baker, D. M. H., Head, J. W., Collins, G. S., & Potter, R. W. K. (2016). The formation of peak-ring basins: Working hypotheses and path forward in using observations to constrain models of impact-basin formation. *Icarus*, *273*, 146–163. https://doi.org/10.1016/j.icarus.2015.11.033

Cheek, L. C., Donaldson Hanna, K. L., Pieters, C. M., Head, J. W., & Whitten, J. L. (2013). The distribution and purity of anorthosite across the Orientale basin: New perspectives from Moon Mineralogy Mapper data. *Journal of Geophysical Research: Planets*, *118*, 1805–1820. https://doi.org/10.1002/jgre.20126

Collins, G. S., Melosh, H. J., & Ivanov, B. A. (2004). Damage and deformation in numerical impact simulations. *Meteoritics and Planetary Science*, *39*(2), 217–231. https://doi.org/10.1111/j.1945-5100.2004.tb00337.x

Collins, G. S., Melosh, H. J., Morgan, J. V., & Warner, M. R. (2002). Hydrocode simulations of Chicxulub crater collapse and peak-ring formation. *Icarus*, *157*(1), 24–33. https://doi.org/10.1006/icar.2002.6822

Hartmann, W. K., & Kuiper, G. P. (1962). Concentric structures surrounding lunar basins. *Communications of the Lunar and Planetary Laboratory*, *1*, 51–66.

Johnson, B. C., Blair, D. M., Collins, G. S., Melosh, H. J., Freed, A. M., Taylor, G. J., … Zuber, M. T. (2016). Formation of the Orientale lunar multiring basin. *Science*, *354*(6311), 441–444. https://doi.org/10.1126/science.aag0518

Kramer, G. Y., Kring, D. A., Nahm, A. L., & Pieters, C. M. (2013). Spectral and photogeologic mapping of Schrödinger basin and implications for post-south pole-Aitken impact deep subsurface stratigraphy. *Icarus*, *223*(1), 131–148. https://doi.org/10.1016/j.icarus.2012.11.008

Kring, D. A., Kramer, G. Y., Collins, G. S., Potter, R. W. K., & Chandnani, M. (2016). Peak-ring structure and kinematics from a multi-disciplinary study of the Schrödinger impact basin. *Nature Communications*, *7*, 13161. https://doi.org/10.1038/ncomms13161

Le Feuvre, M., & Wieczorek, M. A. (2011). Nonuniform cratering of the Moon and a revised crater chronology of the inner solar system. *Icarus*, *214*(1), 1–20. https://doi.org/10.1016/j.icarus.2011.03.010

Melosh, H. J. (1989). *Impact Cratering. A Geological Process*, *Oxford Monographs on Geology and Geophysics* (pp. 245). New York: Oxford University Press.

Melosh, H. J., Freed, A. M., Johnson, B. C., Blair, D. M., Andrews-Hanna, J. C., Neumann, G. A., … Zuber, M. T. (2013). The origin of lunar mascon basins. *Science*, *340*(6140), 1552–1555. https://doi.org/10.1126/science.1235768

Miljković, K., Collins, G. S., Wieczorek, M. A., Johnson, B. C., Soderblom, J. M., Neumann, G. A., & Zuber, M. T. (2016). Subsurface morphology and scaling of lunar impact basins. *Journal of Geophysical Research: Planets*, *121*, 1695–1712. https://doi.org/10.1002/2016JE005038

Miljković, K., Wieczorek, M. A., Collins, G. S., Laneuville, M., Neumann, G. A., Melosh, H. J., … Zuber, M. T. (2013). Asymmetric distribution of lunar impact basins caused by variations in target properties. *Science*, *342*(6159), 724–726, https://doi.org/10.1126/science.1243224

Miljković, K., Wieczorek, M. A., Collins, G. S., Solomon, S. C., Smith, D. E., & Zuber, M. T. (2015). Excavation of the mantle in basin-forming impact events on the Moon. *Earth and Planetary Science Letters*, *409*, 243–251. https://doi.org/10.1016/j.epsl.2014.10.041

Morgan, J. V., Gulick, S. P. S., Bralower, T., Chenot, E., Christeson, G., Claeys, P., … Zylberman, W. (2016). The formation of peak-rings in large impact craters. *Science*, *354*(6314), 878–882. https://doi.org/10.1126/science.aah6561

Murray, J. B. (1980). Oscillating peak model of basin and crater formation. *Moon and the Planets*, *22*(3), 269–291. https://doi.org/10.1007/BF01259285

Neumann, G. A., Zuber, M. T., Wieczorek, M. A., Head, J. W., Baker, D. H. M., Solomon, S. C., … Kiefer, W. S. (2015). Lunar impact basins revealed by Gravity Recovery and Interior Laboratory measurements. *Science Advances*, *1*(9), e1500852. https://doi.org/10.1126/sciadv.1500852

Pierazzo, E., Artemieva, N., Asphaug, E., Baldwin, E. C., Cazamias, J., Coker, R., … Wünnemann, K. (2008). Validation of numerical codes for impact and explosion cratering: Impacts on strengthless and metal targets. *Meteoritics and Planetary Science*, *43*(12), 1917–1938. https://doi.org/10.1111/j.1945-5100.2008.tb00653.x

Potter, R. W. K., Kring, D. A., & Collins, G. S. (2013). Quantifying the attenuation of structural uplift beneath large lunar craters. *Geophysical Research Letters*, *40*, 5615–5620. https://doi.org/10.1002/2013GL057829

Potter, R. W. K., Kring, D. A., & Collins, G. S. (2015). Scaling of basin-sized impacts and the influence of target temperature. In G. R. Osinski & D. A. Kring (Eds.), *Meteorite Impacts and Planetary Evolution V*, *Geological Society of America Special Paper 518* (pp. 99–113). https://doi:10.1130/2015.2518(06)

Potter, R. W. K., Kring, D. A., Collins, G. S., Kiefer, W. S., & McGovern, P. J. (2012). Estimating transient crater size using the crustal annular bulge: Insights from numerical modeling of lunar basin-scale impacts. *Geophysical Research Letters*, *39*, L18203. https://doi.org/10.1029/2012GL052981

Potter, R. W. K., Kring, D. A., Collins, G. S., Kiefer, W. S., & McGovern, P. J. (2013). Numerical modeling of the formation and structure of the Orientale impact basin. *Journal of Geophysical Research: Planets*, *118*(5), 963–979. https://doi.org/10.1002/jgre.20080

Spudis, P. D. (1993). *The Geology of Multi-Ring Impact Basins* (pp. 277). New York: Cambridge University Press. https://doi.org/10.1017/CBO9780511564581

Wieczorek, M. A., Neumann, G. A., Nimmo, F., Kiefer, W. S., Taylor, G. J., Melosh, H. J., … Zuber, M. T. (2013). The crust of the Moon as seen by GRAIL. *Science*, *339*(6120), 671–675. https://doi.org/10.1126/science.1231530

Wood, C. A., & Head, J. W. (1976). Comparison of impact basins on mercury, Mars and the Moon, Proc. Lunar Sci. Conf. 7, 3629–3651.

Wünnemann, K., Collins, G. S., & Melosh, H. J. (2006). A strain-based porosity model for use in hydrocode simulations of impacts and implications for transient crater growth in porous targets. *Icarus*, *180*(2), 514–527. https://doi.org/10.1016/j.icarus.2005.10.013

Yamamoto, S., Nakamura, R., Matsunaga, T., Ogawa, Y., Ishihara, Y., Morota, T., … Haruyama, J. (2010). Possible mantle origin of olivine around lunar impact basins detected by SELENE. *Nature Geoscience*, *3*(8), 533–536. https://doi.org/10.1038/ngeo897

Zhu, M.-H., Wünnemann, K., & Potter, R. W. K. (2015). Numerical modeling of the ejecta distribution and formation of the Orientale basin on the Moon. *Journal of Geophysical Research: Planets*, *120*, 2118–2134. https://doi.org/10.1002/2015JE004827

Zuber, M. T., Smith, D. E., Neumann, G. A., Goossens, S., Andrews-Hanna, J. C., Head, J. W., … Yuan, D.-N. (2016). Gravity field of the Orientale basin from the Gravity Recovery and Interior Laboratory mission. *Science*, *354*(6311), 438–441. https://doi.org/10.1126/science.aag0519